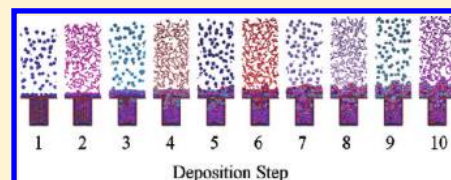


# Layer-by-Layer Assembly of Polyelectrolyte Chains and Nanoparticles on Nanoporous Substrates: Molecular Dynamics Simulations

Jan-Michael Y. Carrillo and Andrey V. Dobrynin\*

Polymer Program, Institute of Materials Science and Department of Physics, University of Connecticut, Storrs, Connecticut 06269, United States

**ABSTRACT:** We performed molecular dynamics simulations of a multilayered assembly of oppositely charged polyelectrolyte chains and nanoparticles on porous substrates with cylindrical pores. The film was constructed by the sequential adsorption of oppositely charged species in a layer-by-layer fashion from dilute solutions. The multilayer assembly proceeds through surface overcharging after the completion of each deposition step. The substrate overcharging fraction fluctuates around 0.5 for nanoparticle–polyelectrolyte systems and around 0.4 for polyelectrolyte–polyelectrolyte systems. The surface coverage increases linearly with the number of deposition steps. The rate of surface coverage increases as a function of the number of deposition step changes when the pore is blocked. The closing of the pore occurs from the pore entrance for nanoparticle–polyelectrolyte systems. In the case of polyelectrolyte–polyelectrolyte systems, the pore plug is formed inside the pore and then spreads toward the pore ends.



## INTRODUCTION

The layer-by-layer (LbL) deposition of charged macromolecules is a valuable technique for the fabrication of multifunctional polymeric nanocomposites.<sup>1–11</sup> This is achieved by the sequential dipping of a charged substrate into solutions with cationic or anionic species. LbL assembly was used for the fabrication of ultrathin films made from synthetic polyelectrolytes, DNA, proteins, charged nanoparticles, and other supramolecular species. (For a review, see refs 1, 2, and 6–9.) Experimental studies,<sup>1–11</sup> computer simulations,<sup>12–24</sup> and theoretical studies<sup>25–28</sup> of the multilayer assembly have shown that the stable layer assembly proceeds through surface overcharging during each deposition step and that the film buildup demonstrates a linear growth with both the layer thickness and the surface coverage increase linearly with the number of deposition steps. The multilayer assembly process was significantly sped up by utilizing spraying,<sup>7,29–33</sup> spin-coating,<sup>7,27,34</sup> and printing<sup>35</sup> techniques for layer deposition. These methods have another advantage over the conventional dipping procedure because they require only small amounts of solution to cover large surface areas.

Recently, porous substrates were used as templates for LbL assembly.<sup>8,10,36–42</sup> Rubner's group<sup>43</sup> deposited polyelectrolyte multilayers of poly(allylamine hydrochloride) (PAH) and poly(sodium 4-styrenesulfonate) (PSS) onto track-etched polycarbonate membranes (TEPC). They observed that the LbL-modified membranes were responsive to pH variations, demonstrating large discontinuous changes in the transmembrane flux. This indicated that the multilayers formed within the cylindrical pores of TEPC membranes exhibit the discontinuous swelling/deswelling transition. Such stimuli-responsive membranes have the potential for applications in selective separation, in stimuli-responsive mechanochemical valves, in biosensor development, and in multifunctional substrate design. (See ref 8 for a review.) The LbL assembly on nanoporous templates was also

implemented for the “synthesis” of polyelectrolyte nanotubes under optimal deposition conditions.<sup>36,42,44,45</sup> The nanotubes were extracted by dissolving the surrounding membrane material. By changing the number of LbL deposition cycles and polyelectrolyte pairs used for LbL assembly, one can control the thickness, composition, and mechanical properties of the nanotubes.<sup>44</sup>

The analysis of the film thickness inside the cylindrical pores showed that the mechanism of LbL assembly in confined spaces is qualitatively different from that observed on the flat substrates.<sup>36,40–43</sup> There are two different regimes in the LbL growth inside pores. At the initial stage of the LbL assembly process, the layer thickness grows linearly with an increasing number of deposition steps. This linear growth regime was followed by the slow growth regime<sup>42</sup> or even by the saturation regime<sup>40,41</sup> when the layer thickness did not change during the later stages of the deposition process. Our computer simulations<sup>46</sup> of the LbL assembly of nanoparticles within cylindrical pores have shown that the hindrance of the film growth inside nanopores occurs long before the remaining open pore size becomes smaller than the size of the adsorbing nanoparticles. This is pointed out on the electrostatic origin of the saturation regime of the film growth inside nanopores. It was argued that the electrostatic barrier at the pore entrance can completely inhibit LbL assembly, resulting in the saturation of the LbL layer thickness inside a pore after just a few deposition steps. However, our molecular dynamics simulations dealt with nanoparticles that are rigid objects. The important question that remained unanswered in our simulations was how does the chemical structure of the species influence the LbL assembly in confined spaces? In particular, will the

**Received:** October 7, 2011

**Revised:** December 6, 2011

**Published:** December 7, 2011

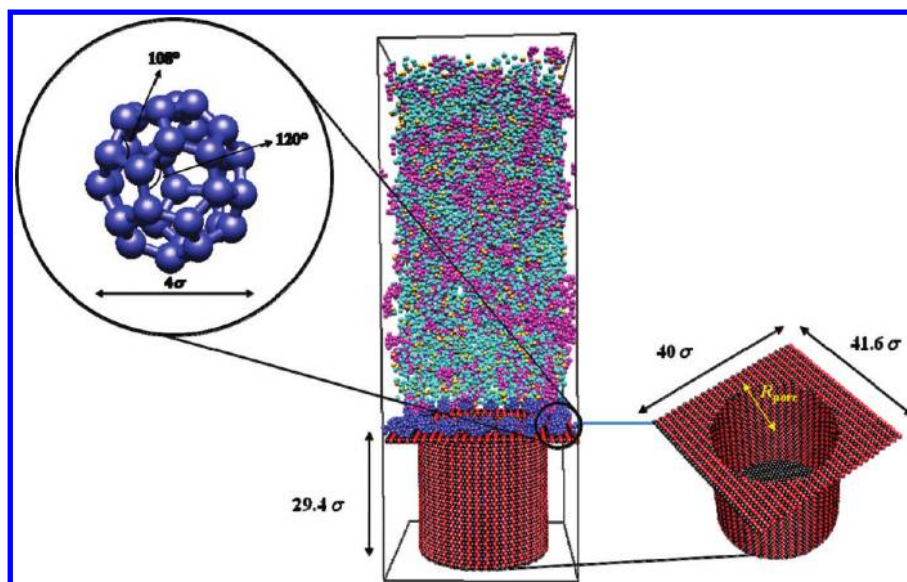


**Figure 1.** Snapshot of the simulation box of the nanoparticle–polyelectrolyte system at the beginning of the second deposition step. Blue nanoparticles and cyan counterions are negatively charged. Red surface atoms, magenta polyelectrolytes, and orange counterions are positively charged. Neutral substrate particles are black. A C32 fullerene-like nanoparticle is shown on the left.

mechanism of the saturation of the layer thickness inside cylindrical pores be the same for nanoparticles and flexible chains. To address these issues, we have performed molecular dynamics simulations of the LbL assembly of polyelectrolyte–nanoparticle and polyelectrolyte–polyelectrolyte films on porous substrates with cylindrical pores of different diameters.

## ■ MODEL AND SIMULATION DETAILS

We performed molecular dynamics simulations<sup>47,48</sup> of the multilayer assembly of oppositely charged nanoparticles and polyelectrolyte chains on porous substrates with different pore sizes. The simulation setup was similar to the one used in our previous simulations of the LbL deposition of charged nanoparticles.<sup>46</sup> The simulation box had dimensions of  $L_x \times L_y \times L_z = 40\sigma \times 41.6\sigma \times 110.9\sigma$  (Figure 1). The adsorbing positively charged surface was placed at  $z = 0\sigma$  and was modeled by a hexagonally packed lattice of particles (beads) with diameter  $\sigma$ . (Note that the bottom of the simulation box was located at  $z = -29.9\sigma$ .) The substrate had pores with radii equal to  $R_{\text{pore}} = 5.09\sigma$ ,  $10.03\sigma$ , and  $14.96\sigma$ . All surface beads forming the bottom of the pore were neutral. Every second bead belonging to the substrate and side walls of the cylindrical pores carried a univalent charge.

In our simulations, nanoparticles had a diameter equal to  $4\sigma$  and consisted of 32 charged beads, each with a diameter of  $\sigma$  (Figure 1). Polyelectrolyte chains were modeled by bead–spring chains consisting of 32 charged beads.

The short-range interactions between all particles in the system were described by the truncated-shifted Lennard-Jones (LJ) potential

$$U_{\text{LJ}}(r_{ij}) = \begin{cases} 4\epsilon_{\text{LJ}} \left[ \left( \frac{\sigma}{r_{ij}} \right)^{12} - \left( \frac{\sigma}{r_{ij}} \right)^6 - \left( \frac{\sigma}{r_{\text{cut}}} \right)^{12} + \left( \frac{\sigma}{r_{\text{cut}}} \right)^6 \right] & r \leq r_{\text{cut}} \\ 0 & r > r_{\text{cut}} \end{cases} \quad (1)$$

where  $r_{ij}$  is the distance between the  $i$ th and  $j$ th beads and  $\sigma$  is the bead diameter chosen to be the same regardless of the bead type. The cutoff distance,  $r_{\text{cut}} = 2.5\sigma$ , was selected for

surface–nanoparticle, surface–polyelectrolyte, polyelectrolyte–nanoparticle, polyelectrolyte–polyelectrolyte, and nanoparticle–nanoparticle pairs, and  $r_{\text{cut}} = (2)^{1/6}\sigma$  was selected for other short-range interactions. The interaction parameter  $\epsilon_{\text{LJ}}$  was equal to  $0.5k_{\text{B}}T$  for polyelectrolyte–nanoparticle, polyelectrolyte–polyelectrolyte, and nanoparticle–nanoparticle pairs, and interaction parameter  $\epsilon_{\text{LJ}}$  was set equal to  $k_{\text{B}}T$  for all other pairs, where  $k_{\text{B}}$  is the Boltzmann constant and  $T$  is the absolute temperature. The choice of parameters for surface–nanoparticle, surface–polyelectrolyte, polyelectrolyte–nanoparticle, polyelectrolyte–polyelectrolyte, and nanoparticle–nanoparticle LJ potentials corresponds to the effective short-range attraction, and the interaction potential with  $r_{\text{cut}} = (2)^{1/6}\sigma$  corresponds to purely repulsive interactions.

The connectivity of beads in nanoparticles and polyelectrolyte chains was maintained by the finite extension nonlinear elastic (FENE) potential<sup>49</sup>

$$U_{\text{FENE}}(r) = -\frac{1}{2}k_{\text{spring}}R_{\text{max}}^2 \ln \left( 1 - \frac{r^2}{R_{\text{max}}^2} \right) \quad (2)$$

with a spring constant of  $k_{\text{spring}} = 100k_{\text{B}}T/\sigma^2$  and a maximum bond length of  $R_{\text{max}} = 1.5\sigma$ . The repulsive part of the bond potential was modeled by the truncated-shifted LJ potential with  $r_{\text{cut}} = (2)^{1/6}\sigma$  and  $\epsilon_{\text{LJ}} = k_{\text{B}}T$ .

The shape of the nanoparticles was fixed by imposing the harmonic angle potential

$$U_{\text{bend}}(\theta) = \frac{1}{2}k_{\text{bend}}(\theta - \theta_0)^2 \quad (3)$$

where  $\theta$  is an angle between two consecutive bonds and the bending constant is  $k_{\text{bend}} = 200k_{\text{B}}T/\text{rad}^2$ . The value of the valence angle  $\theta_0$  was equal to  $108^\circ$  for pentagons and  $120^\circ$  for hexagons (Figure 1).

The interaction between any two charged particles (beads) with charge valences of  $q_i$  and  $q_j$  that are separated by a distance

$r_{ij}$  is given by the Coulomb potential

$$U_{\text{coul}}(r_{ij}) = k_B T \frac{l_B q_i q_j}{r_{ij}} \quad (4)$$

where  $l_B = e^2/\epsilon k_B T$  is the Bjerrum length, defined as the length scale at which the Coulomb interaction between two elementary charges  $e$ , in a dielectric medium with the dielectric constant  $\epsilon$ , is equal to the thermal energy  $k_B T$ . In our simulations, the value of the Bjerrum length  $l_B$  was set to  $\sigma$ . Note that in aqueous solutions at room temperature ( $T = 300$  K), the value of the Bjerrum length is equal to  $l_B = 7.14$  Å. Counterions from the charged surface, nanoparticles, and polyelectrolyte chains were explicitly included in our simulations. All charged particles in our simulations were monovalent ions.

The particle–particle–particle–mesh (PPPM) method<sup>50</sup> for the slab geometry, with the correction term implemented in LAMMPS<sup>47</sup> with the sixth-order charge interpolation scheme and an estimated accuracy between  $10^{-4}$  and  $10^{-5}$ , was used for calculations of the electrostatic interactions. In this method, the 2-D periodic images of the system are periodically replicated along the  $z$  direction with a distance of  $L = 3L_z$  between their boundaries.<sup>51</sup>

For simulations of each deposition step, we used a constant number of particles, volume, and temperature ensemble (NVT) with periodic boundary conditions in the  $x$  and  $y$  directions. Constant temperature was maintained by coupling the system to a Langevin thermostat. The equation of motion of the  $i$ th particle was

$$m \frac{d\vec{v}_i(t)}{dt} = \vec{F}_i(t) - \xi \vec{v}_i(t) + \vec{F}_i^R(t) \quad (5)$$

where  $\vec{v}_i(t)$  is the particle velocity and  $\vec{F}_i(t)$  is the net deterministic force acting on  $i$ th particle of mass  $m$ .  $\vec{F}_i^R(t)$  is the stochastic force with a zero average value of  $\langle \vec{F}_i^R(t) \rangle = 0$  and  $\delta$ -functional correlations of  $\langle \vec{F}_i^R(t) \vec{F}_i^R(t') \rangle = 6\xi k_B T \delta(t - t')$ . Friction coefficient  $\xi$  was set to  $\xi = 0.143m/\tau_{\text{LJ}}$ , where  $\tau_{\text{LJ}}$  is the standard LJ time  $\tau_{\text{LJ}} = \sigma(m/\epsilon_{\text{LJ}})^{1/2}$ . The velocity Verlet algorithm with a time step of  $\Delta t = 0.01\tau_{\text{LJ}}$  was used for the integration of the equations of motion (eq 5). All particles had a unit mass.

We performed simulations of the layer-by-layer assembly of nanoparticle–polyelectrolyte and polyelectrolyte–polyelectrolyte systems. The simulation procedure of the multilayer assembly by the sequential deposition of charged nanoparticles or polyelectrolyte chains was similar to that previously reported in refs 17 and 46 and is briefly described below. At the beginning of the first deposition step,  $M_1 = 180$  negatively charged nanoparticles or polyelectrolyte chains consisting of 32 monomers (beads) each, corresponding to a monomer concentration above the substrate of  $c = 0.043\sigma^{-3}$ , together with their counterions and surface counterions were added to the simulation box. The simulation run continues until the completion of  $2 \times 10^4 \tau_{\text{LJ}}$  (details in ref 46). To facilitate adsorption, we have implemented stirring steps.<sup>46,52</sup> In these simulations, we have uniformly redistributed the remaining unadsorbed nanoparticles or polyelectrolyte chains and counterions in the simulation box every  $4 \times 10^3 \tau_{\text{LJ}}$ . Such a redistribution forced nanoparticles or polyelectrolyte chains to refill a depletion zone (the region close to the substrate with low nanoparticle or polyelectrolyte density).

After the completion of the first simulation run (the dipping step), unadsorbed nanoparticles or polyelectrolyte chains were removed (the rinsing step). The unadsorbed nanoparticles or polyelectrolyte chains were separated from the adsorbed ones by using a cluster algorithm with a cutoff radius equal to  $2.0\sigma$ .<sup>46</sup> The cluster analysis was performed by analyzing the matrix of distances between all

beads in the system. After the completion of the simulation run (deposition step), only the counterions needed for the compensation of the excess charge on the growing film were kept in the simulation box to maintain the electroneutrality of the system.

At the beginning of the second deposition step, the simulation box was refilled with  $M_2 = M_1 = 180$  oppositely charged polyelectrolyte chains together with their counterions, resulting in the concentration of newly added species to be the same as before,  $c = 0.043\sigma^{-3}$ . This was followed by the simulation run (dipping step) lasting another  $2 \times 10^4 \tau_{\text{LJ}}$ . The duration of the each simulation run was sufficient for the system to reach a steady state. We repeated the dipping and rinsing steps to model 10 deposition steps. The final  $5 \times 10^3 \tau_{\text{LJ}}$  was used for data collection. We have increased the simulation box size along the  $z$  direction by the average increment in the layer thickness  $\Delta z$  after each deposition step, starting with the third deposition step. This allowed us to maintain approximately the same volume accessible to nanoparticles or polyelectrolyte chains on top of the growing film during the whole deposition process.

All simulations were performed using LAMMPS<sup>47</sup> with GPU acceleration.<sup>53</sup>

## SIMULATION RESULTS

Figure 2 shows our results for the evolution of the film structure made of charged nanoparticles and flexible polyelectrolyte chains

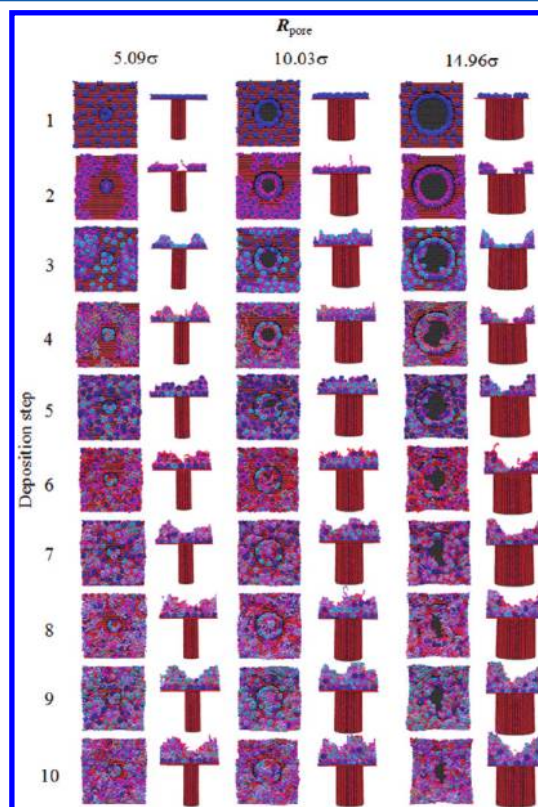


**Figure 2.** Evolution of the film structure made of charged nanoparticles and polyelectrolyte chains. Snapshots are taken after the completion of deposition steps 1–10. The positively charged beads of the substrate are shown in red, and neutral beads are shown in black. The nanoparticles or polyelectrolytes deposited on the substrate during different deposition steps are (1) blue, (2) magenta, (3) Dodger blue, (4) chestnut, (5) dark blue, (6) dark red, (7) slate blue, (8) lavender, (9) steel blue, and (10) purple.

during the deposition process. We used different colors to highlight charged species adsorbed during different deposition



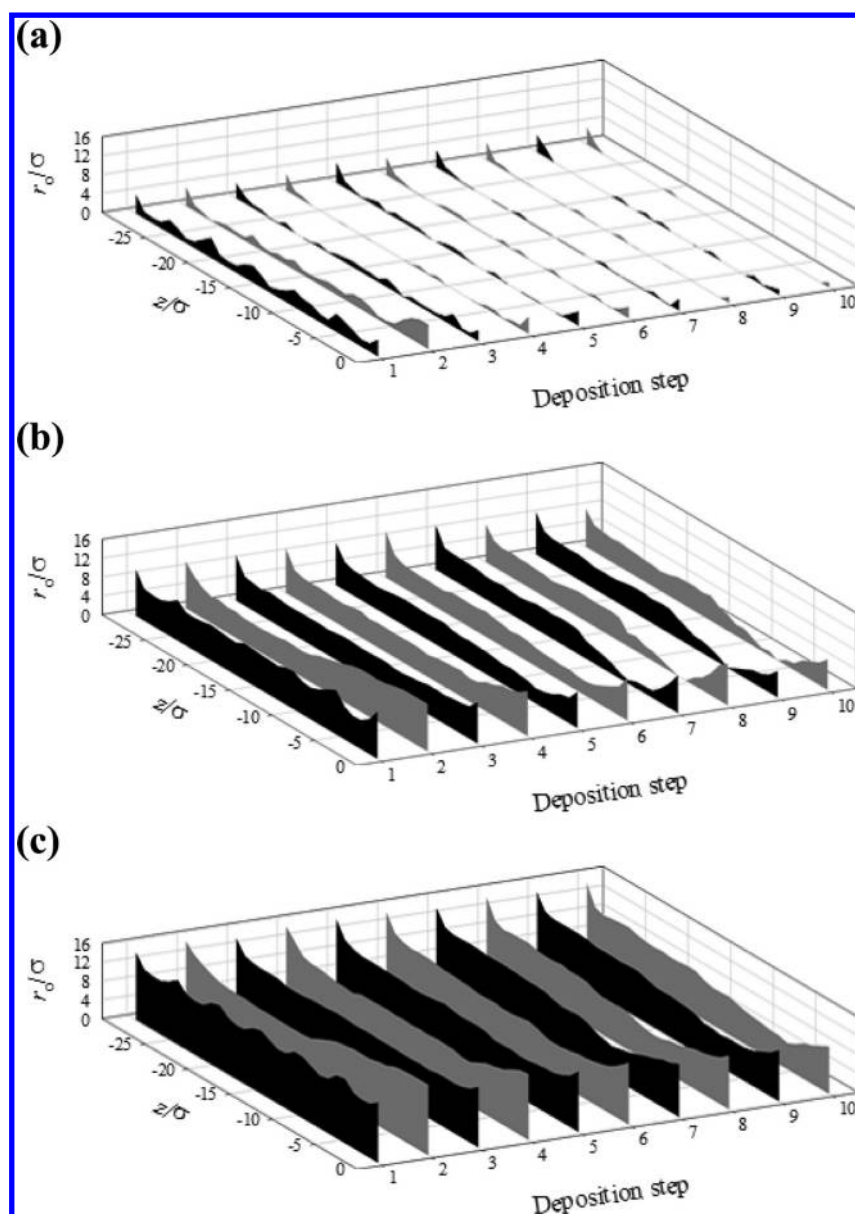


**Figure 3.** Effective pore size  $r_0$  as a function of the pore depth  $z$  obtained during different deposition steps for nanoparticle–polyelectrolyte systems for substrates with pore sizes,  $R_{\text{pore}}$  of  $5.09\sigma$  (a),  $10.03\sigma$  (b), and  $14.96\sigma$  (c).

steps. During the first deposition step, negatively charged nanoparticles adsorbed onto a positively charged substrate. The strong electrostatic repulsion between nanoparticles forces them to organize into an almost perfect hexagonal lattice. Note that even in the case of the largest pore size this nanoparticle arrangement is preserved. After the completion of the second deposition step, the positively charged chains glue together negatively charged nanoparticles, freeing the substrate. The aggregates of nanoparticles and polyelectrolytes are formed at the periphery of the simulation box, thus emptying the space surrounding a pore.

Inside a pore, the aggregates are usually formed closer to the pore entrance. This is evident from the distribution of the effective pore radius along the pore depth shown in Figure 3. (The effective pore radius  $r_0$  along a pore axis was obtained from the open area  $S_0$  of the pore at location  $z$ , where  $r_0 = (S_0/\pi)^{1/2}$ .) The empty space on the substrate and on the pore wall is filled by negatively charged nanoparticles adsorbed during the third deposition step. It is also important to point out that the complexes formed between

negatively charged nanoparticles and positively charged chains are not frozen. In Figure 2, we see that nanoparticles deposited during the first deposition step cover empty spots on the substrate together with nanoparticles deposited during the third deposition step whereas nanoparticles deposited during the third deposition step form complexes with polyelectrolyte chains. The process of complexation between nanoparticles and polyelectrolyte chains continues throughout the entire deposition process. It is also interesting that there is funnel formation around the pore.

Only three deposition steps were required to close the smallest pore with  $R_{\text{pore}} = 5.09\sigma$  (Figure 3). The largest pore remained open even after the completion of the 10th deposition step. It is also evident from Figure 3 that the pore size varies along the pore axis. For the pore with  $R_{\text{pore}} = 10.03\sigma$ , the plug is beginning to form close to the pore entrance after the completion of the sixth deposition step and the pore is blocked after the completion of the seventh deposition step, during which adsorbing nanoparticles tightly fit in a pore. This precludes the penetration of

the nanoparticles deep inside a pore, keeping the remainder of the pore length located below  $z \approx -10.0\sigma$  open.

The polymer surface coverage and surface overcharging on porous substrates demonstrate behavior qualitatively similar to that observed in simulations of the LbL assembly on substrates without pores (Figures 4 and 5). The surface coverage  $\Gamma$

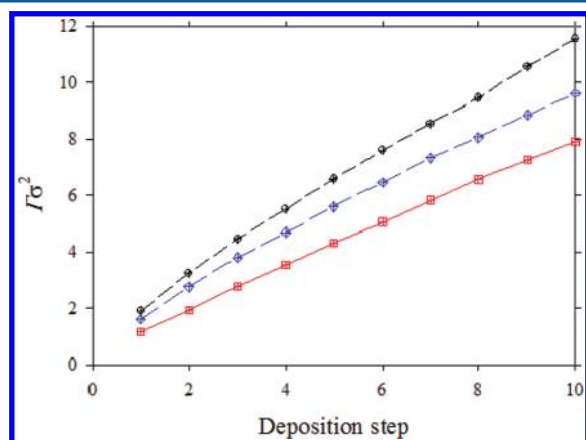


**Figure 4.** Dependence of the surface coverage  $\Gamma$ , defined as the number of adsorbed beads per unit area, on the number of deposition steps for nanoparticle-polyelectrolyte films deposited on substrates with different pore sizes:  $R_{\text{pore}} = 5.09\sigma$  ( $\square$ ),  $R_{\text{pore}} = 10.03\sigma$  ( $\diamond$ ), and  $R_{\text{pore}} = 14.96\sigma$  ( $\circ$ ).

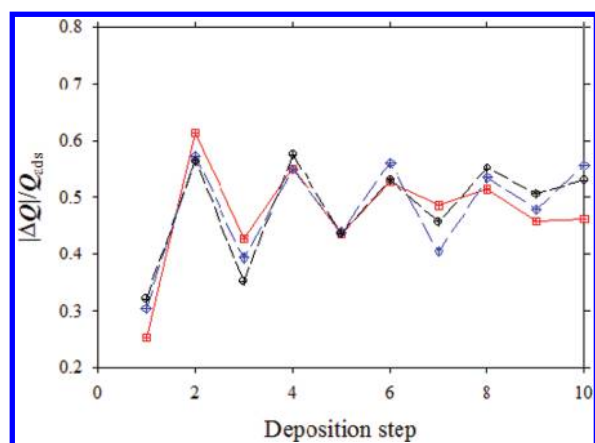


**Figure 5.** Overcharging fractions as a function of the number of deposition steps for nanoparticle-polyelectrolyte systems. The notation is the same as in Figure 4.

increases monotonically with an increasing number of deposition steps. The surface coverage also increases with increasing pore size. The increase in the surface coverage with pore size is a manifestation of the effect of the film growth inside pores. Smaller pores have a smaller access area for film deposition than do larger pores. For intermediate pore size  $R_{\text{pore}} = 10.03\sigma$ , one can identify the change in the slope of the surface coverage dependence with an increasing number of deposition steps, indicating the correlation of the change in the slope with the pore closing. Figure 5 shows our results for overcharging fraction  $|\Delta Q|/Q_{\text{ads}}$ , defined as a ratio of the absolute value of the film overcharging  $|\Delta Q|$  (excess of positively or negatively charged beads including those belonging to the substrate within a growing film at a given deposition step) to the absolute value of the total charge  $Q_{\text{ads}} = 32 N_{\text{ads}}(s)$  carried by all  $N_{\text{ads}}(s)$  species (nanoparticles or polyelectrolyte chains)

adsorbed during the  $s$ th deposition step. This quantity oscillates around 0.5. Thus, approximately half of the adsorbed nanoparticles or polyelectrolyte chains neutralize the film, and the second half provides excess charge for further film buildup.

Experimentally, the LbL assembly within a pore is characterized by the average film thickness or the average size of the pore opening. In Figure 6, we show the dependence of

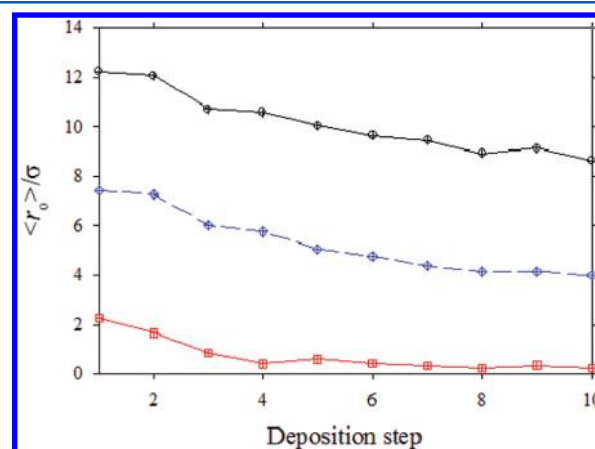


**Figure 6.** Evolution of the average pore size  $\langle r_0 \rangle$  with the number of deposition steps for nanoparticle-polyelectrolyte systems. The notation is the same as in Figure 4.

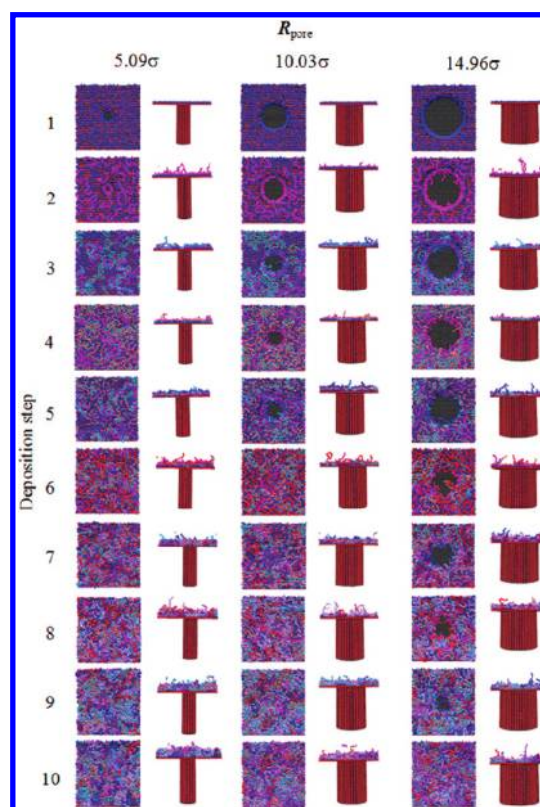


**Figure 7.** Evolution of the film structure made of polyelectrolyte chains. Snapshots are taken after the completion of deposition steps 1–10. The positively charged beads of the substrate are shown in red, and neutral beads are shown in black. The polyelectrolyte chains deposited on the substrate during different deposition steps are (1) blue, (2) magenta, (3) Dodger blue, (4) chestnut, (5) dark blue, (6) dark red, (7) slate blue, (8) lavender, (9) steel blue, and (10) purple.

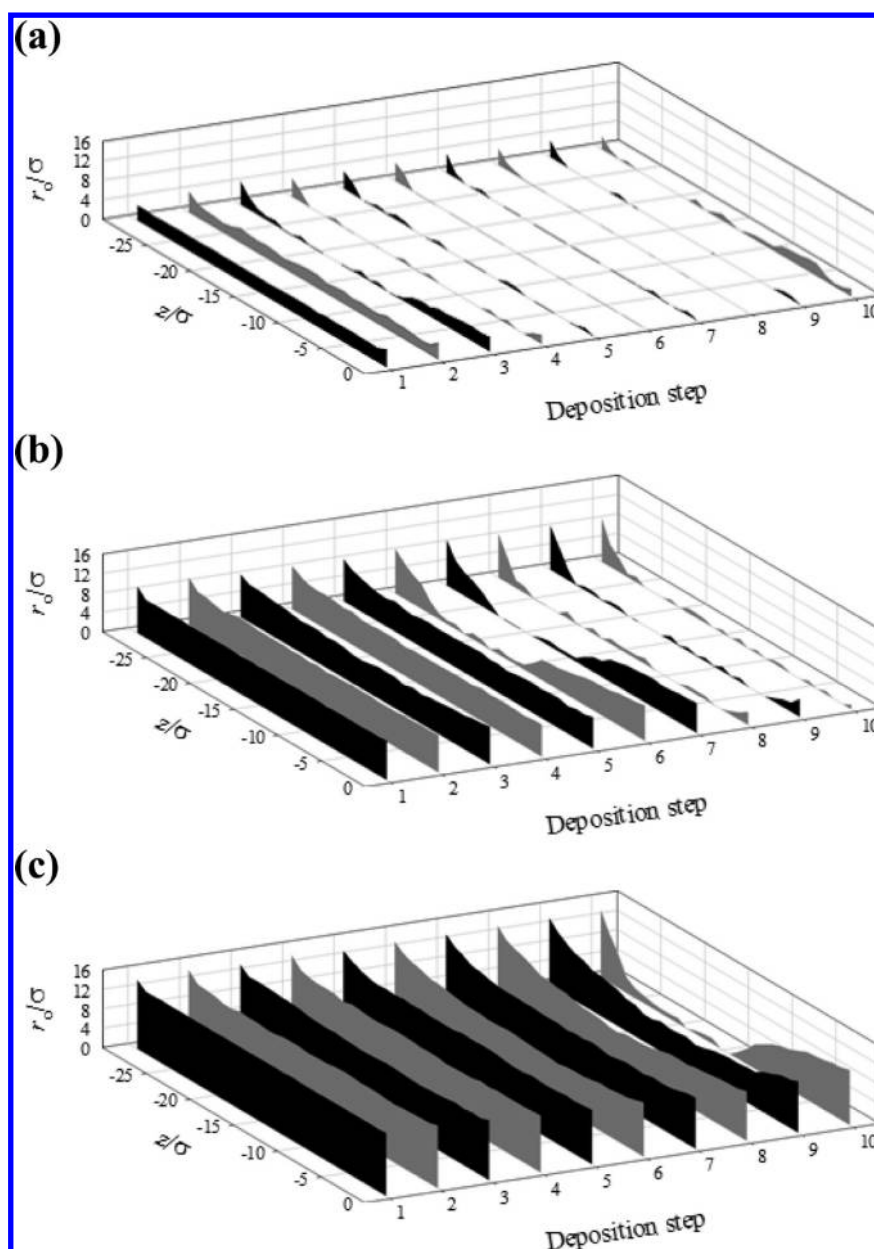


**Figure 8.** Effective pore size  $r_p$  as a function of the pore depth  $z$  obtained during different deposition steps for polyelectrolyte–polyelectrolyte systems for substrates with pore sizes,  $R_{\text{pore}}$ , of  $5.09\sigma$  (a),  $10.03\sigma$  (b), and  $14.96\sigma$  (c).

the average pore radius as a function of the number of deposition steps. The average was calculated along the pore axis. The smallest pore,  $R_{\text{pore}} = 5.09\sigma$ , is completely closed after two deposition step. The size of the pore with  $R_{\text{pore}} = 10.03\sigma$  first decreases with an increasing number of deposition steps and then saturates. Saturation of the average pore size is an indication that no new charged species penetrate a pore and that the mass of the film built inside a pore remains unchanged. The average size of the largest pore decreases throughout the entire deposition process.

To elucidate further the effect of how structural differences of the adsorbing species influence film formation on a porous substrate, we have performed simulations of the LbL assembly of polyelectrolyte chains. Figure 7 shows the evolution of the film structure during the deposition process. After the first deposition step, adsorbed polyelectrolyte chains uniformly cover the substrate and the surfaces of the pores. During the second deposition step, oppositely charged chains form complexes but the surface is still

well covered with a polymeric film. This is qualitatively different to what we have seen for the film made of nanoparticles and polyelectrolytes (Figure 2). Inside the pore, the polymers are uniformly distributed along the pore (Figure 8). Starting from third deposition step, the plug begins to form in the middle of the smallest pore with  $R_{\text{pore}} = 5.09\sigma$ . This plug increases in length during the fourth and fifth deposition steps. The pore remains closed until the ninth deposition step. The small opening appears during the tenth deposition step, indicating that chains are not frozen inside a pore and continue to move around.

The pore with  $R_{\text{pore}} = 10.03\sigma$  remains open during the first five deposition steps. The plug inside a pore appears during the sixth deposition step, and it grows in size during the seventh and eighth deposition steps. After the eighth deposition step, the pore is filled with polyelectrolytes. Our largest pore remains open through nine deposition steps (Figures 7 and 8). Polyelectrolyte chains fill the bottom of the pore during the 10th deposition step.



However, the top part of the pore is still open. The differences between the closing of the pore in polyelectrolyte–polyelectrolyte (P–P) and nanoparticle–polyelectrolyte (N–P) systems are interesting. In N–P systems, the blocking of the pore occurs from the top part of the pore. Thus, complexes between polyelectrolyte chains and nanoparticles form a plug. The rearrangement of such complexes is a much more difficult task than the diffusion of the flexible chains in concentrated solutions of oppositely charged polyelectrolytes covering the pore walls.

The polymer surface coverage grows linearly with the number of deposition steps (Figure 9). One still can see a

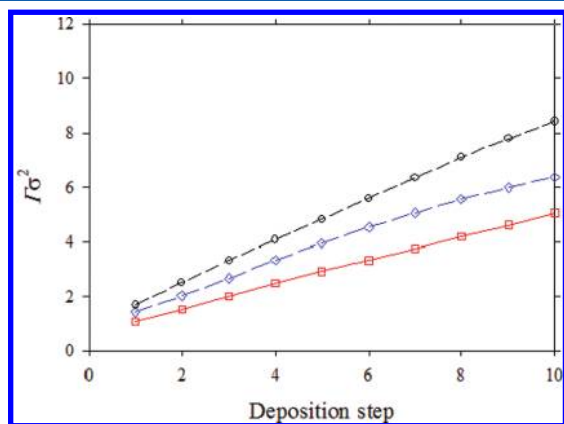


**Figure 9.** Dependence of the polymer surface coverage  $\Gamma$  on the number of deposition steps for polyelectrolyte–polyelectrolyte films deposited on the substrates with different pore sizes:  $R_{\text{pore}} = 5.09\sigma$  ( $\square$ ),  $R_{\text{pore}} = 10.03\sigma$  ( $\diamond$ ), and  $R_{\text{pore}} = 14.96\sigma$  ( $\circ$ ).

change in the slope of the polymer surface coverage for the LbL film growing on a substrate with  $R_{\text{pore}} = 10.03\sigma$  occurring at the seventh deposition step. This correlates with the pore-closing event. The overcharging fraction (Figure 10) begins to oscillate

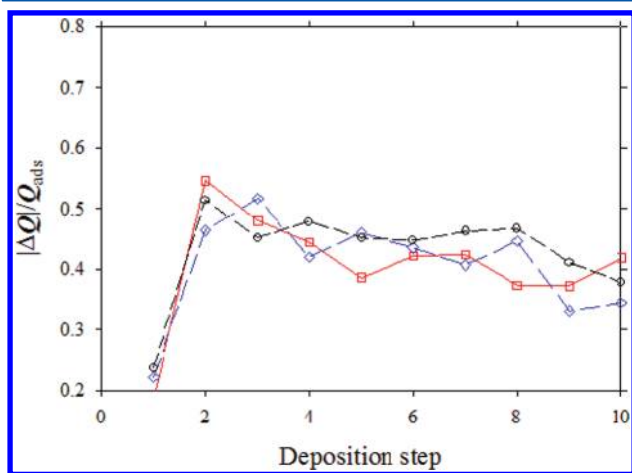


**Figure 10.** Dependence of the overcharging fraction on the number of deposition steps for polyelectrolyte–polyelectrolyte systems. The notation is the same as in Figure 9.

around 0.4 during later stages of the deposition process. This shift is due to the filling of the pore by neutral polyelectrolyte complexes. The average pore size decreases with increasing number of deposition steps and then saturates for substrates with  $R_{\text{pore}} = 5.09\sigma$  and  $10.03\sigma$ . The saturation of the average pore size is due to pore closing. The average size of the largest pore continuously decreases during the entire deposition process.

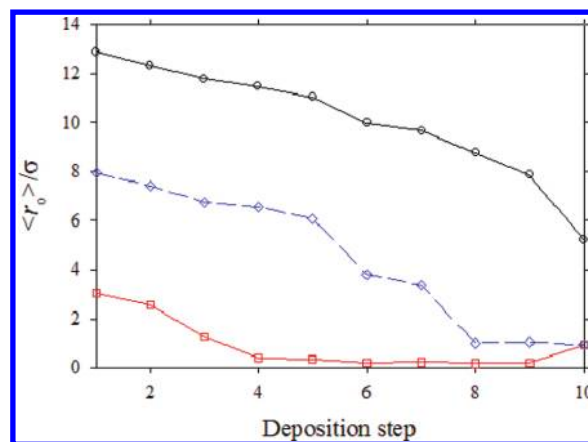


**Figure 11.** Evolution of the average pore size  $\langle r_0 \rangle$  with the number of deposition steps for polyelectrolyte–polyelectrolyte systems. The notation is the same as in Figure 9.

## CONCLUSIONS

We have performed molecular dynamics simulations of the LbL assembly of nanoparticle–polyelectrolyte and polyelectrolyte–polyelectrolyte films on porous substrates with different pore sizes. Macroscopic film properties such as the surface coverage and overcharging fraction demonstrate features similar to those observed for LbL assembly on substrates without pores. The surface coverage increases with the increasing number of deposition steps independently of the size of the pore. However, one can identify a change in the growth rate of the surface coverage with the number of deposition steps. This change in the growth rate is associated with the pore-closing event. The pore-closing mechanism is different in N–P and P–P systems. In the N–P systems, the plug closing the pore begins to form at the pore entrance whereas for P–P systems it first appears inside the pore and then propagates toward both ends of the pore. Note that the change in the surface coverage growth rate can be directly tested in experiments and can be correlated with the pore-closing events by measuring the dependence of the substrate permeability<sup>43</sup> on the number of deposition steps.

In the N–P systems, the overcharging fraction oscillates around 0.5, thus half of the newly adsorbing species is used for film neutralization and the other half is used for the re-creation of the film charge. Note that similar behavior was observed in our simulations of the nanoparticle–nanoparticle systems.<sup>46</sup> For P–P systems, the overcharging fraction oscillates around 0.4, which is due to the filling of the pore with neutral polyelectrolyte complexes. Also, the surface coverage for P–P systems is more uniform than for N–P systems. Thus, flexible chains are more adaptive in adjusting their conformations to cover imperfections in the film structure.

## ACKNOWLEDGMENTS

We are grateful to the National Science Foundation for financial support under grant DMR-1004576.

## REFERENCES

- (1) Decher, G. *Science* **1997**, *277*, 1232–1237.
- (2) Schonhoff, M. *J. Phys.: Condens. Matter* **2003**, *15*, R1781–R1808.
- (3) Schonhoff, M. *Curr. Opin. Colloid Interface Sci.* **2003**, *8*, 86–95.
- (4) Sukhorukov, G.; Fery, A.; Mohwald, H. *Prog. Polym. Sci.* **2005**, *30*, 885–897.

- (5) Sukhishvili, S. A.; Kharlampieva, E.; Izumrudov, V. *Macromolecules* **2006**, *39*, 8873–8881.
- (6) Lutkenhaus, J. L.; Hammond, P. T. *Soft Matter* **2007**, *3*, 804–816.
- (7) Ariga, K.; Hill, J. P.; Ji, Q. *Phys. Chem. Chem. Phys.* **2007**, *9*, 2319–2340.
- (8) Ariga, K.; Ji, Q. M.; Hill, J. P.; Vinu, A. *Soft Matter* **2009**, *5*, 3562–3571.
- (9) Srivastava, S.; Kotov, N. A. *Acc. Chem. Res.* **2008**, *41*, 1831–1841.
- (10) Kerdjoudj, H.; Berthelemy, N.; Boulmedais, F.; Stoltz, J. F.; Menu, P.; Voegel, J. C. *Soft Matter* **2010**, *6*, 3722–3734.
- (11) Becker, A. L.; Johnston, A. P. R.; Caruso, F. *Small* **2010**, *6*, 1836–1852.
- (12) Panchagnula, V.; Jeon, J.; Dobrynin, A. V. *Phys. Rev. Lett.* **2004**, *93*.
- (13) Panchagnula, V.; Jeon, J.; Rusling, J. F.; Dobrynin, A. V. *Langmuir* **2005**, *21*, 1118–1125.
- (14) Messina, R. *Macromolecules* **2004**, *37*, 621–629.
- (15) Patel, P. A.; Jeon, J.; Mather, P. T.; Dobrynin, A. V. *Langmuir* **2005**, *21*, 6113–6122.
- (16) Patel, P. A.; Jeon, J.; Mather, P. T.; Dobrynin, A. V. *Langmuir* **2006**, *22*, 9994–10002.
- (17) Jeon, J.; Panchagnula, V.; Pan, J.; Dobrynin, A. V. *Langmuir* **2006**, *22*, 4629–4637.
- (18) Abu-Sharkh, B. J. *Chem. Phys.* **2005**, *123*, 114907–1–6.
- (19) Abu-Sharkh, B. *Langmuir* **2006**, *22*, 3028–3034.
- (20) Dobrynin, A. V.; Rubinstein, M. *Prog. Polym. Sci.* **2005**, *30*, 1049–1118.
- (21) Dobrynin, A. V. *Curr. Opin. Colloid Interface Sci.* **2008**, *13*, 376–388.
- (22) Messina, R. *J. Phys.: Condens. Matter* **2009**, *21*, 113102.
- (23) Cerda, J. J.; Qiao, B.; Holm, C. *Eur. Phys. J. Spec. Top.* **2009**, *177*, 129–148.
- (24) Cerda, J. J.; Qiao, B. F.; Holm, C. *Soft Matter* **2009**, *5*, 4412–4425.
- (25) Netz, R. R.; Joanny, J. F. *Macromolecules* **1999**, *32*, 9013–9025.
- (26) Park, S. Y.; Rubner, M. F.; Mayes, A. M. *Langmuir* **2002**, *18*, 9600–9604.
- (27) Lefaux, C. J.; Zimmerlin, J. A.; Dobrynin, A. V.; Mather, P. T. *J. Polym. Sci., Part B: Polym. Phys.* **2004**, *42*, 3654–3666.
- (28) Shafir, A.; Andelman, D. *Eur. Phys. J. E* **2006**, *19*, 155–162.
- (29) Izquierdo, A.; Ono, S. S.; Voegel, J. C.; Schaaf, P.; Decher, G. *Langmuir* **2005**, *21*, 7558–7567.
- (30) Krogman, K. C.; Lowery, J. L.; Zacharia, N. S.; Rutledge, G. C.; Hammond, P. T. *Nat. Mater.* **2009**, *8*, 512–518.
- (31) Kolasinska, M.; Krastev, R.; Gutberlet, T.; Warszynski, P. *Langmuir* **2009**, *25*, 1224–1232.
- (32) Nogueira, G. M.; Banerjee, D.; Cohen, R. E.; Rubner, M. F. *Langmuir* **2010**, *27*, 7860–7867.
- (33) Popa, G.; Boulmedais, F.; Zhao, P.; Hemmerle, J.; Vidal, L.; Mathieu, E.; Felix, O.; Schaaf, P.; Decher, G.; Voegel, J. C. *ACS Nano* **2010**, *4*, 4792–4798.
- (34) Patel, P. A.; Dobrynin, A. V.; Mather, P. T. *Langmuir* **2007**, *23*, 12589–12597.
- (35) Andres, C. M.; Kotov, N. A. *J. Am. Chem. Soc.* **2010**, *132*, 14496–14502.
- (36) Alem, H.; Blondeau, F.; Glinel, K. *Macromolecules* **2007**, *40*, 3366–3372.
- (37) Kamci, D.; Ajiro, H.; Hongo, C.; Akashi, M. *Chem. Lett.* **2008**, *37*, 332–333.
- (38) Wang, Y.; Angelatos, A. S.; Caruso, F. *Chem. Mater.* **2008**, *20*, 848–858.
- (39) Steinhart, M. Supramolecular Organization of Polymeric Materials in Nanoporous Hard Templates. In *Self-Assembled Nanomaterials II: Nanotubes*; Shimizu, T., Ed.; Advances in Polymer Science; Springer: Berlin, 2008; Vol. 220, pp 123–187.
- (40) Kim, J. Y.; DeRocher, J. P.; Mao, P.; Han, J.; Cohen, R. E.; Rubner, M. F. *Chem. Mater.* **2010**, *22*, 6409–6415.
- (41) Lazzara, T. D.; Lau, K. H. A.; Abou-Kandil, A. I.; Caminade, A. M.; Majoral, J. P.; Knoll, W. *ACS Nano* **2010**, *4*, 3909–3920.
- (42) Roy, C. J.; Dupont-Gillain, C.; Demoustier-Champagne, S.; Jonas, A. M.; Landoulsi, J. *Langmuir* **2010**, *26*, 3350–3355.
- (43) Lee, D.; Nolte, A. J.; Kunz, A. L.; Rubner, M. F.; Cohen, R. E. *J. Am. Chem. Soc.* **2006**, *128*, 8521–8529.
- (44) Cuenot, S.; Alem, H.; Louarn, G.; Demoustier-Champagne, S.; Jonas, A. M. *Eur. Phys. J. E* **2008**, *25*, 343–348.
- (45) Cho, Y.; Lee, W.; Jhon, Y. K.; Genzer, J.; Char, K. *Small* **2011**, *6*, 2683–2689.
- (46) Carrillo, J.-M. Y.; Dobrynin, A. V. *ACS Nano* **2011**, *5*, 3010–3019.
- (47) Plimpton, S. J. *J. Comput. Phys.* **1995**, *117*, 1–19, [lammmps.sandia.gov](http://lammmps.sandia.gov).
- (48) Frenkel, D.; Smit, B. *Understanding Molecular Simulations*; Academic Press: New York, 2002.
- (49) Kremer, K.; Grest, G. S. *J. Chem. Phys.* **1990**, *92*, 5057–5086.
- (50) Hockney, R. W.; Eastwood, J. W. *Computer Simulations Using Particles*; Hilger-IOP: Bristol, U.K., 1988.
- (51) Crozier, P. S.; Rowley, R. L.; Henderson, J. W. *J. Chem. Phys.* **2001**, *114*, 7513.
- (52) Carrillo, J. M. Y.; Dobrynin, A. V. *Langmuir* **2007**, *23*, 2472–2482.
- (53) Brown, W. M.; Wang, P.; Plimpton, S. J.; Tharrington, A. N. *Comput. Phys. Commun.* **2011**, *182*, 898–911.